Research Article

Tectonic, hydrogeologic, and climatic controls on Late Holocene dune formation, China Lake basin, Indian Wells Valley, California, USA

Nicholas Lancaster[a]* (iD), Steven N. Bacon[a], Thomas F. Bullard[a], Christina M. Neudorf[a], Amanda K. Keen-Zebert[a], David L. Decker[a] and Matthew L. Boggs[b]

[a]Desert Research Institute, Naval Earth Science and Engineering Program, Reno, Nevada, USA and [b]Naval Air Warfare Center—Weapons Division, U.S. Navy, China Lake, California, USA

Abstract

Analysis of patterns of faulting and hydrogeology, stratigraphic and sedimentologic studies, and luminescence dating of aeolian deposits in China Lake basin provide new perspectives on the origins and development of Late Holocene dunes and sand ramps in the seismically active Indian Wells Valley of eastern California. Aeolian dune and sand sheet deposits were sourced from alluvial material derived from granitic rocks of the south-eastern Sierra Nevada and are concentrated in areas with sand-stabilizing phreatophyte vegetation influenced by high groundwater levels along the active oblique-normal Little Lake and Paxton Ranch faults, which locally form barriers to groundwater flow. Three episodes of sand accumulation are recognized (2.1 ± 0.1 to 2.0 ± 0.1 ka, 1.8 ± 0.2 to 1.6 ± 0.2 ka, and 1.2 ± 0.1 to 0.9 ± 0.1 ka) during conditions in which sediment supplied to the basin during periods of enhanced rainfall and runoff was subsequently reworked by wind into dunes and sand ramps at the transition to more arid periods. Understanding the role tectonics plays in influencing the hydrogeology of seismically active lake basins provides insights to accurately interpret landscape evolution and any inferences made on past hydroclimate variability in a region.

Keywords: Mojave Desert, China Lake, Aeolian, Holocene, Tectonics, Groundwater hydrology

(Received 1 April 2021; accepted 10 September 2021)

INTRODUCTION

Dunes and dune fields in the arid western U.S. are typically small and relatively isolated in comparison to some of the major aeolian dune systems elsewhere in the world (e.g., Sahara, Arabia, Australia). Isolated dunes and small dune fields in the southwestern U.S. are associated with nearby sand sources, typically distal alluvial fan and axial-valleys settings of desert bolsons, ephemeral streams, and playa floors of former pluvial lake basins. Controls on the extent of these dune fields typically are related to source-sediment supply and, in many instances, physical barriers to sand transport, such as mountain ranges and areas of dense vegetation. The depth to local groundwater that can support phreatophytic vegetation that may stabilize dune fields can be influenced by geologic structure, including faults. However, there are few studies of the association of areas of aeolian sand accumulation and the influence of tectonics and groundwater hydrology.

The northern Mojave Desert of California contains some of the most active fault systems in the western U.S. It is also characterized by small, isolated source-bordering dune fields, in contrast to the more extensive dune fields and sand transport systems of the central and southern Mojave (Lancaster, 2020). Many of these small dune fields are located adjacent to sediment sources in local playa basins and alluvial drainages (Lancaster and Mahan, 2012; Munroe et al., 2017) and are important centers of biodiversity, hosting endemic sand-obligate plants and insects (e.g., Pavlik, 1989; Epps et al., 1998), as well as important archaeological sites (e.g., Quade, 1986). Understanding the controls, origins, and history of these dune systems therefore has wide significance for the ecology and cultural history of the region, yet the history and relations to both hydrogeologic influences caused by active faulting and climate change of most of these dune fields are poorly understood.

The primary goals of this investigation are: (1) to demonstrate that the locations of dune fields in the China Lake basin are primarily influenced by a unique active tectonic setting, which has controlled the hydrogeologic system, which in turn governs the distribution of phreatophytic vegetation and stability of aeolian deposits and features; and (2) to provide an example of relations between the formation of dunes and temporal changes in sediment supply from alluvial and fluvial-deltaic sources in China Lake basin. In order to accomplish this, we: (1) describe the stratigraphy and sedimentology at two study sites in the lake basin; (2) present new luminescence ages for aeolian deposits; (3) develop associations between the location of prominent dune fields in
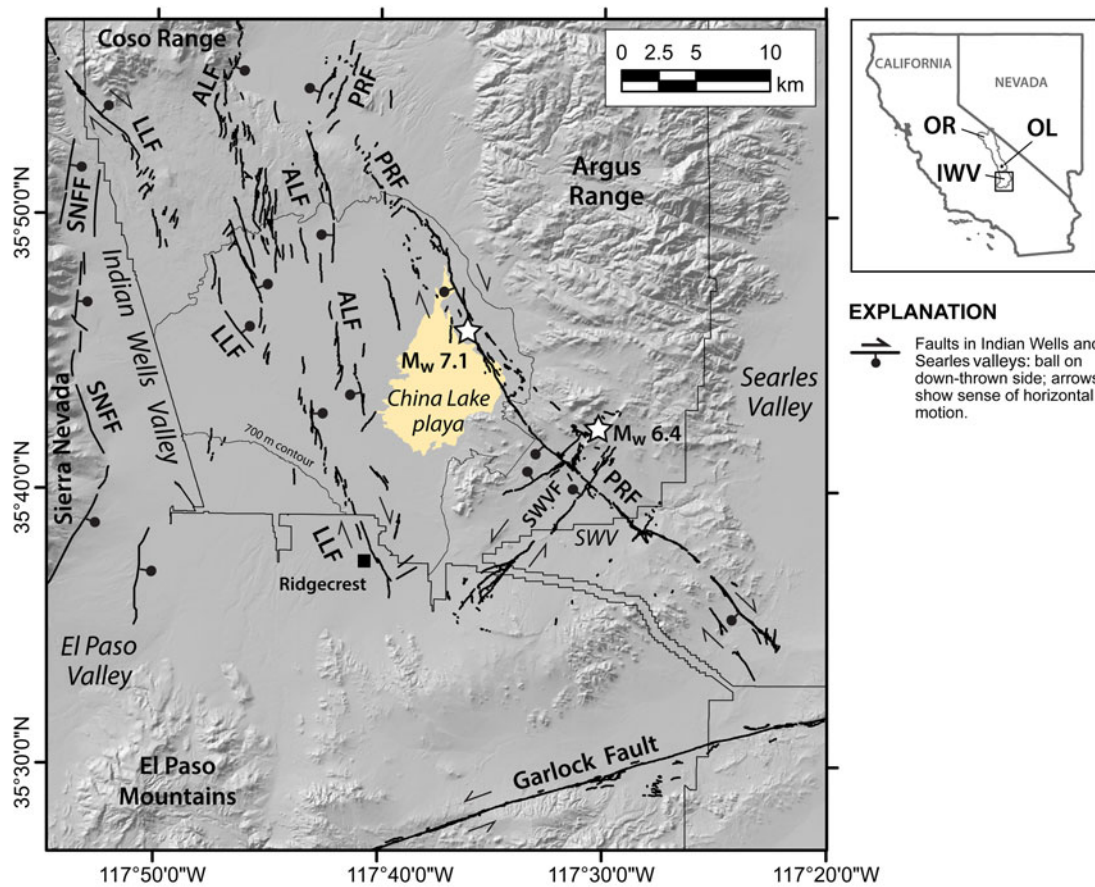
Figure 1. Map of the Indian Wells Valley showing the present extent of China Lake playa, physiographic features, and location of major fault systems in the valley. Faults shown on the map include: ALF = Airport Lake fault; LLF = Little Lake fault; and SNFF = Sierra Nevada frontal fault (modified after USGS, 2016). The surface rupture and epicenters of the AD 2019 Ridgecrest earthquake sequence are also shown: PRF = Paxton Ranch fault and SWVF = Salt Wells Valley fault (DuRoss et al., 2020; Ponti et al., 2020; Thompson Jobe et al., 2020). Inset map shows location of study area: OR = Owens River watershed including Owens Lake (OL); IWV = Indian Wells Valley watershed. Naval Air Weapons Station China Lake (NAWSCL) installation boundary is shown with a thin line. The 700-m-elevation contour defines the extent of geomorphic mapping within NAWSCL and the boundary of Figure 2.

the lake basin and their tectonic and hydrogeologic settings; and (4) evaluate temporal correspondence between aeolian deposition in China Lake basin and Late Holocene aeolian records in the Intermountain West and the lake level record at Owens Lake (100 km to the NNW) to identify trends in hydroclimate variability related to climate change.

GEOLOGIC AND HYDROLOGIC SETTING

The study area is within the China Lake basin, which is a terminal playa basin located in the Indian Wells Valley along the eastern escarpment of the southern Sierra Nevada in eastern California and the northern Mojave Desert (Fig. 1). The Indian Wells Valley watershed includes Rose Valley, El Paso Valley, and China Lake basin, which collectively are tectonic grabens along the eastern escarpment of the southern Sierra Nevada. The watershed has a drainage area of ∼3390 km^2 and is bounded by the Sierra Nevada on the west, the Argus Range and Searles Valley on the east, the Coso Range on the north, and the El Paso Mountains on the south (Fig. 1). The southern Sierra Nevada is the highest range in the watershed, with elevations up to ∼2990 m. Although the range has a strong orographic effect on the distribution of precipitation across the valley, the overall elevations are too low to accumulate perennial snow, and geomorphic evidence

along the crest indicates a lack of glaciation (e.g., Moore and Moring, 2013).

The south-eastern Sierra Nevada Mountains are composed of mostly Mesozoic granitoid rocks that supply alluvial fans from the west and south with abundant detrital quartz and feldspar. The El Paso Mountains are composed of Permian to Jurassic gabbro and granitic plutons overlain by Tertiary sedimentary and volcanic rocks. The Coso Range consists of a weathered granitoid core, with a cap of Quaternary volcanic rocks associated with the Coso volcanic field. The southern Argus Range is comprised of Mesozoic sedimentary and metasedimentary sequences and Mesozoic granitic intrusions (Dunne and Walker, 2004) and provides sediments to the northeastern part of the lake basin. Much of the western piedmont alluvial fans and interior of the southern Argus Range is covered with sand sheets and migrating dune deposits derived from the playa basin.

Tectonic setting

The Indian Wells Valley tectonic graben is located within a seismically active region of California north of the Garlock fault, which is referred to as the southern Walker Lane belt. This area of active transtensional faulting is located to the east of the Sierra Nevada microplate at the western edge of the extensional
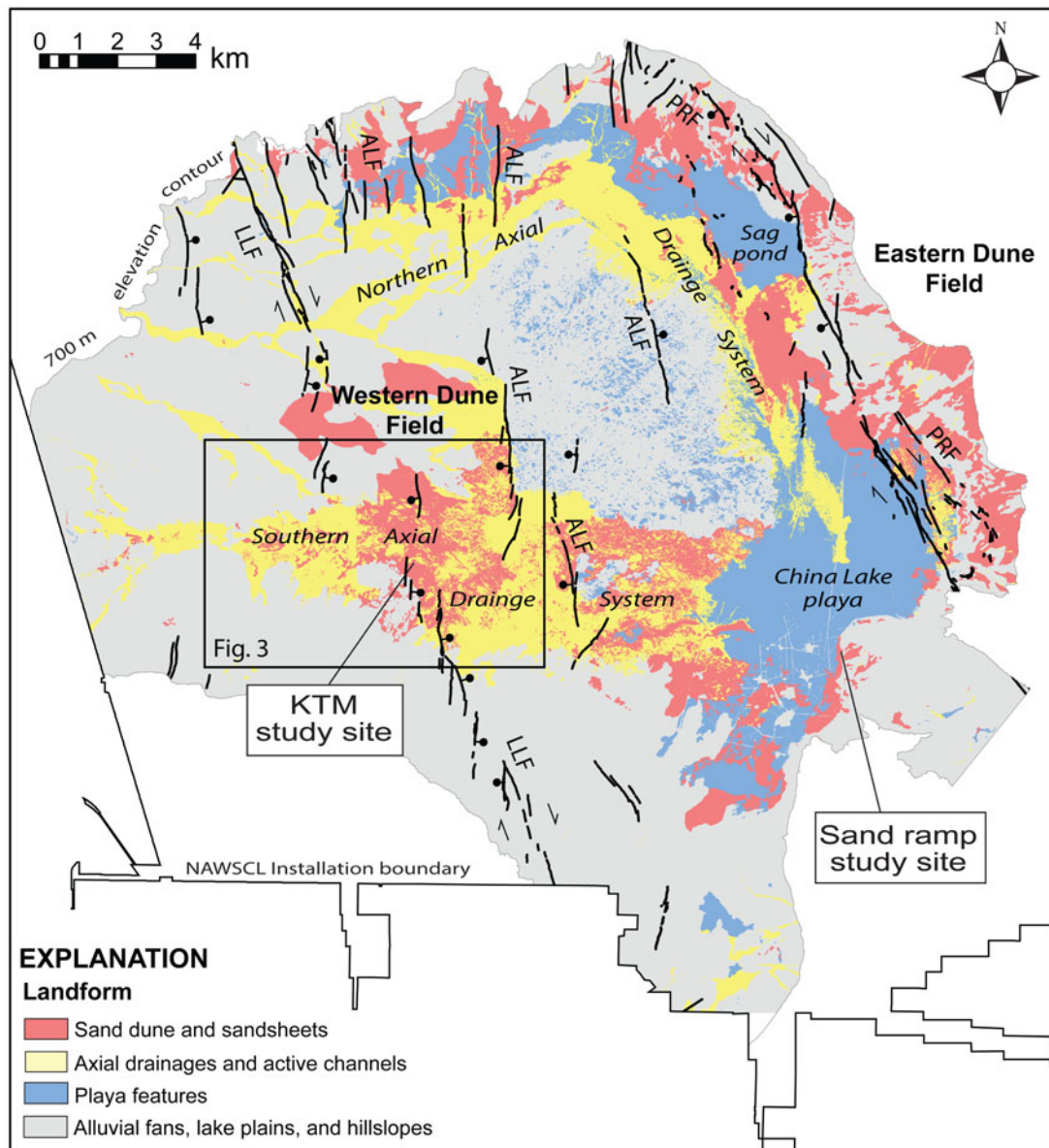
Figure 2. Map showing stratigraphic study sites within Naval Air Weapons Station China Lake (NAWSCL) in relation to the western and eastern dune fields and northern and southern axial drainage systems in China Lake basin. Generalized landforms are from geomorphic mapping below the 700-m-elevation contour within NAWSCL (Bullard et al., 2019; see Fig. 1). Fault traces of the active Little Lake fault (LLF), Airport Lake fault (ALF) (modified after USGS, 2016), and Paxton Ranch fault (PRF) (DuRoss et al., 2020; Ponti et al., 2020) are also shown in relation to dune fields.

Basin and Range Province (e.g., Dokka and Travis, 1990; Wesnousky, 2005). The Indian Wells Valley is bounded on the west by the normal Sierra Nevada frontal fault system and on the south by the active left-lateral Garlock fault. The floor of the valley and China Lake basin is crossed by active, northerly striking faults that merge towards the north with the Sierra Nevada frontal fault system and Coso volcanic field (e.g., Roquemore and Zellmer, 1987; Monastero et al., 2002; Amos et al., 2013) (Fig. 1).

The active faults in the valley include the Little Lake fault (LLF) and Airport Lake fault (ALF) (Bryant and Hart, 2007). The LLF was previously considered the principal fault system in the valley and is characterized as an oblique, right-lateral fault with down-to-the-east normal displacement, whereas the ALF is an oblique, right-lateral fault with mostly down-to-the-west

normal displacement where it bifurcates from LLF in the north-central part of the lake basin prior to switching to predominately down-to-the-east normal displacement along the Coso Range (Zellmer and Roquemore, 1997) (Fig. 1). Both faults are expressed at the surface across the lake basin as a distributed zone of short, en-echelon scarps formed in part by two historical ground-rupturing earthquakes: the first in AD 1982 on the LLF (Roquemore and Zellmer, 1987) and the second in AD 1995 on the ALF (Hauksson et al., 1995) (Fig. 1). Although the surface rupture traces were relatively short (~2–3 km) and showed little offsets, the surface ruptures were associated with earthquakes of M4.9 and 5.8, respectively (Hauksson et al., 1995).

The complexity of the slip distribution within Indian Wells Valley was recently demonstrated by the AD 2019 Ridgecrest earthquake sequence along two orthogonal-striking faults,

including a dominantly left-lateral and northeast-striking rupture in the Mw 6.4 foreshock and a dominantly right-lateral and northwest-striking rupture in the Mw 7.1 mainshock (Fig. 1). The Mw 6.4 foreshock produced an ~18 km long rupture within Salt Wells Valley, whereas the Mw 7.1 earthquake produced an ~50-km-long surface rupture along the eastern margin of China Lake basin and into Salt Wells and Searles valleys. The earthquakes ruptured previously unidentified fault zones that have been named the Paxton Ranch fault (PRF) and Salt Wells Valley fault (SWVF) (DuRoss et al., 2020; Ponti et al., 2020; Thompson Jobe et al., 2020) (Fig. 1). Two prominent dune fields are located within the western and eastern sectors of China Lake basin that are coincident with the active LLF-ALF and PRF zones (Fig. 2).

Climatic Setting

The Indian Wells Valley lies in the rain shadow of the southern Sierra Nevada and has a hot, arid climate. Mean annual temperature is 26.7°C, with a monthly range from 15–16°C in December–January to 39–40°C in July–August. Annual rainfall averages 108 mm and occurs mainly in the winter months (January–March), with a wide variation from year to year, (e.g., 249 mm in 1992 to 19 mm in 1994) (https://wrcc.dri.edu/cgi-bin/cliMAIN.pl?ca1733).

The wind regime of China Lake basin is dominated by winds from the south through west directions. This is also the sector from which the strongest winds blow. Winds from this sector account for ~41–68% of all winds over the year, with the maximum from this sector occurring in April (https://wrcc.dri.edu/cgi-bin/rawMAIN.pl?caKNID). The distribution of wind speed is related to the seasonal pattern of frontal systems, in which cyclogenesis and topographic effects of the Sierra Nevada and the Tehachapi Mountains farther to the west-southwest are maximized in late winter and early spring (Jewell and Nicoll, 2011). Rare, but high-magnitude, northerly wind events are associated with the passage of cold fronts; while strong southerly wind events occur ahead of an upper level trough off the California coast (Shiyuan et al., 2008).

Sand transport potential in the China Lake basin is dominated by winds from the south through west sector, and this sector accounts for as much as 83% of annual potential sand movement. The annual sand drift potential averages 364 vector units, an intermediate energy wind regime (after Fryberger and Dean, 1979). The ratio between the total potential sand transport from all directions and the resultant vector magnitude is 0.70, classifying the sand transport potential regime as wide unimodal.

METHODS

Two stratigraphic sites on the Naval Air Weapons Station China Lake (NAWSCL) were studied to establish ages of investigated aeolian deposits, as well as to evaluate the tectonic, climatic, and hydrogeologic factors that control the formation of prominent vegetated dune fields in the lake basin: (1) a trench in the western dune field, referred to as the KTM study site, was excavated for construction material in the 1960s through ~6 m of aeolian deposits and extending ~4 m below the modern ground surface into alluvial and lacustrine to fluvio-deltaic deposits; and (2) a gully exposure through a sand ramp at ~670 m elevation in the southeastern part of the basin referred to as the Sand Ramp study site (Fig. 2).

Geomorphic mapping

Previous to this study, a detailed geomorphic map (Fig. 2) was developed for the China Lake basin below an elevation of 700 m within NAWSCL (Naval Air Weapons Station China Lake) (Bacon et al., 2019; Bullard et al., 2019). This GIS-based mapping forms the basis for the description and analysis of aeolian landforms in this study.

Stratigraphy

Investigations at the KTM study site included the evaluation of dune ridge sediments and underlying fluvial flood plain and lacustrine to fluvial-deltaic deposits. Sediment exposed in a ~10-m-deep trench were described and sampled for particle size, geochemical analyses, and luminescence dating. A Trimble global positioning system (GPS) Pathfinder® ProXRT receiver with differential correction services was used for elevation control at the site, coupled with a total-station to survey stratigraphic horizons and sample locations on trench walls. A ~2.5-m-deep, hand-auger borehole was also placed at the bottom of the trench to explore deeper stratigraphy.

Aeolian features downwind (east) of the western dune field and the KTM study site also were investigated to potentially link the spatiotemporal extent of Late Holocene sand transport across the lake basin. A 1–2-m-deep gully exposure of aeolian sands and underlying gravels was described and sampled for luminescence dating at the Sand Ramp study site (Fig. 2).

Aeolian sediment analysis

Samples of aeolian sediment were analyzed for particle size using sieving, following pre-treatment to remove organics. Bulk mineralogy was determined using semi-quantitative XRD (X-ray Diffraction) at the Desert Research Institute Soils Laboratory. Calcium carbonate content (wt%) was determined using a pressure calcimeter method (Sherrod et al., 2002) on a subsample of crushed material. Particle size and sorting statistics were calculated using the program Gradistat (Blott and Pye, 2001).

Luminescence dating

Post-IR-IRSL methods were used to directly date aeolian and underlying lacustrine to fluvial-deltaic sediments at the KTM and Sand Ramp study sites. At the KTM site (Fig. 6), nine samples were collected in opaque tubes inserted into sand dune deposits that lacked evidence of bioturbation in the walls of the KTM trench (CL-16-1 to CL-16-9). One sample was collected from a borehole that was hand augured into lacustrine to fluvial-deltaic deposits at the floor of the trench (CL-16-10) (Figs. 5A, 6). At the Sand Ramp site, two samples were collected from depths of 1 m below the shoulder of the channel wall within sandy layers that lacked bioturbation (CL-14-1 to CL-14-2).

Samples were prepared and analyzed at the Desert Research Institute Luminescence Laboratory (DRILL). In situ sampling in tubes ensured no light exposure. Dating was based on the post-IR-IRSL$_{225}$ luminescence dating method (e.g., Rhodes, 2015). This method has been used recently to date aeolian, alluvial, and lacustrine deposits in nearby Owens Lake basin (Bacon et al., 2018, 2019, 2020; Fig. 1). Samples from the KTM site (CL-16-1 through CL-16-10) were dated using multi-grain

aliquots of ~70 grains each. Samples collected from the Sand Ramp site (CL-14-1, CL-14-2) were measured using single grains.

All luminescence sample preparation was conducted in dim red light conditions where all light is filtered through Lee 106 gel filters. The sediment in both ends of the 30 cm long sample tube was removed to a depth of ~3 cm and used for dose rate and water content measurements (see Table S1 of Supplementary Material). The target sample was taken from the middle of the sample tubes and density separated to extract 180–250 μm potassium feldspar grains (hereafter 'feldspar'). The equivalent dose (D_e) for all samples was measured using a modified single aliquot regenerative-dose (SAR) technique (Murray and Wintle, 2000, 2003). In the post-IRIR$_{225}$ SAR approach used, an initial IR stimulation is applied at low (50°C) temperature before D_e measurements are made using IR stimulation at 225°C (e.g., Rhodes, 2015) (see Supplementary Material and Table S1). The low temperature IRSL stimulation depletes the signal originating from unstable traps that gives rise to anomalous fading, thus allowing the subsequent higher temperature IRSL stimulation to preferentially target the signal from traps that are more stable and less susceptible to fading (Thomsen et al., 2008).

With the exception of sample CL-16-7, no fewer than 35 accepted D_e determinations were used in age modeling. Sample D_e distributions were plotted as kernel density estimates and radial plots, and examined for evidence of partial bleaching or mixing between sedimentary units of different ages (Fig. S2). All D_e distributions are near-symmetrical in shape and their over-dispersion values range from 2–11% for multi-grain aliquot data and from 25–29% for single-grain data (Table 1). These characteristics are consistent with those from samples that have been reasonably well bleached prior to deposition (see Arnold et al., 2009, tables 4, 5). Therefore, the equivalent dose, or burial dose (D_b), for each sample was modeled using the central age model (CAM) of Galbraith et al. (1999). Because the post-IRIR$_{225}$ signal measured from the samples in this study suffers from fading, fading rates from a subset of samples were used to correct all luminescence ages for fading using the correction model of Huntley and Lamothe (2001) (see Supplementary Material for details). Luminescence ages are expressed as thousands of years before 2018 (KTM site) and 2015 (Sand Ramp site) and rounded to the nearest 10 years (Table 1).

A bleaching test was conducted on 20 aliquots of multi-grain feldspar aliquots from sample CL-16-6 to assess the likelihood that the post-IRIR$_{225}$ signal was sufficiently exposed to sunlight prior to burial at the KTM and Sand Ramp sites. Aliquots were exposed directly to sunlight for durations of 0 s, 10 s, 1000 s, 10,000 s, and 100,000 s (4 aliquots per duration), then measured using the SAR protocol (see Table S1 and Fig. S2). After 10,000 s (2.8 h), the post-IRIR$_{225}$ signal decreased to 5% of its initial natural signal, and after 100,000 s (27.8 h), the signal was reduced to negligible levels (Fig. S2). This suggests that the post-IRIR$_{225}$ signal from sediments in the China Lake basin are likely to be completely depleted after two days of sun exposure. We consider it likely that ages obtained from aeolian samples in this study have been sufficiently sun-exposed prior to burial and therefore should not yield age over-estimates. The water-lain sediments from lacustrine/deltaic deposits at the KTM site (sample CL-16-10) were likely more prone to partial bleaching prior to deposition. However, any residual dose detected in this sample should have minimal effect on the final age because only 30 min of sun exposure to some grains would still reduce their estimated sample dose of ~64 Gy down to only ~5 Gy. Such a scenario would lead to an age over-estimate of only ~1.5 ka in this sample.

Groundwater data and analysis

Groundwater-level data in areas of the southwestern sector of Indian Wells Valley were obtained from 102 and 194 monitoring wells measured in AD 1920 and 2006, respectively (IWVGA, 2020). These data were used to estimate groundwater conditions in the western dune field. Surfaces of the groundwater table were constructed by interpolating observed water levels at 10-m resolution with a kriging routine in ArcGIS. Maps of groundwater levels for the two time periods were prepared to evaluate the overall position of water levels and rate of change in relation to sand-stabilizing phreatophyte vegetation and active faults. The long-term trend of declining groundwater levels also was evaluated to assess the potential effect on the phreatophyte vegetation community along the LLF and ALF zones from water resource development over the 86-yr period of record.

RESULTS

In this section we first describe the geomorphology of the western dunefield and discuss its relations to patterns of active faulting and the groundwater hydrogeology of the area. We then present data on the stratigraphy, sediments, and luminescence chronology at the KTM and Sand Ramp study sites.

Dune field geomorphology

Dunes in the China Lake basin have formed in two discrete fields that coincide with: (1) an actively deforming graben where the ALF bifurcates from the LLF, and the downstream reach of the southern axial drainage system (western dune field; Figs. 2, 3); and (2) wave-modified fault scarps of the PRF (e.g., Thompson Jobe et al., 2020), areas with springs and a sag pond on the eastern margin of the lake basin, and the downstream reaches of the northern axial drainage system where it discharges onto low-gradient fluvial plains and the playa (eastern dune field; Fig. 2).

The location of the LLF-ALF system and related geometry in the western dune field area forms a structural graben and topographic low that controls shallow groundwater conditions and drainage patterns, which, in turn, influences the distribution and magnitude of fluvial and aeolian deposition. Subsidence in the graben also provides accommodation space for aeolian deposits. A similar relation exists for vegetated dunes within the eastern dune field where dunes have accumulated primarily in vegetated areas bounding a graben of the PRF controlled by shallow groundwater conditions that commonly discharge as seeps and springs, some of which support wetlands. The area downwind of the western dune field and across the playa is devoid of significant sand deposits. Downwind of the eastern playa margin, aeolian sand forms vegetated dunes in the vicinity of the PRF, as well as sand sheets and sand ramps farther to the east along the base and into stream valleys and uplands of the southern Argus Range (Fig. 2).

The most prominent aeolian features in China Lake basin are located in the western dune field and within and immediately adjacent to the LLF-ALF graben (Figs. 2, 3). Aeolian landforms, comprising vegetated sand sheets, with small areas of parabolic and crescentic dunes, overlie Holocene fluvial deposits and late Pleistocene and Holocene lacustrine and playa deposits.

Table 1. Post-IRIR$_{225}$ ages for samples in this study.

Sample	Study site	Depth (m)	Latitude (°N)	Longitude (°W)	Elevation (m asl)	Dating method[1]	N accepted[2] (N analyzed)	OD[3] (%)	Dose rate[4] (Gy/ka)	Equivalent dose[5] (Gy)	Age[6] (ka)
CL-16-1	KTM	1.0	35.72731	117.72731	669	SA	40 (48)	2	3.41 ± 0.18	6.72 ± 0.07	2.12 ± 0.13
CL-16-2	KTM	1.2	35.72731	117.72731	670	SA	37 (39)	8	3.50 ± 0.19	3.81 ± 0.06	1.17 ± 0.07
CL-16-3	KTM	0.5	35.72731	117.72731	671	SA	42 (48)	7	3.47 ± 0.18	3.40 ± 0.05	1.05 ± 0.06
CL-16-4	KTM	0.5	35.72731	117.72731	672	SA	36 (39)	8	3.85 ± 0.19	3.40 ± 0.06	0.94 ± 0.06
CL-16-5	KTM	0.3	35.72731	117.72731	673	SA	41 (48)	10	3.49 ± 0.19	3.49 ± 0.06	1.07 ± 0.07
CL-16-6	KTM	0.4	35.72731	117.72731	673	SA	39 (46)	6	3.56 ± 0.20	3.02 ± 0.04	0.91 ± 0.06
CL-16-7	KTM	0.5	35.72769	117.72660	667	SA	23 (41)	11	3.28 ± 0.17	6.08 ± 0.26	1.99 ± 0.14
CL-16-8	KTM	0.6	35.72769	117.72660	667	SA	35 (40)	8	3.27 ± 0.19	6.40 ± 0.11	2.11 ± 0.14
CL-16-9	KTM	1.0	35.72751	117.72655	668	SA	38 (41)	3	3.30 ± 0.18	3.70 ± 0.04	1.20 ± 0.07
CL-16-10	KTM	1.4	35.72731	117.72731	663	SA	44 (44)	7	3.43 ± 0.27	64.44 ± 0.87	21.01 ± 1.93
CL-14-1	Sand Ramp	1.0	35.707	117.604	669	SG	80 (700)	29	4.09 ± 0.26	6.60 ± 0.25	1.76 ± 0.16
CL-14-2	Sand Ramp	1.0	35.707	117.604	669	SG	78 (700)	25	4.30 ± 0.27	6.42 ± 0.22	1.63 ± 0.15

[1]"SA" refers to D_e determination using single multi-grain aliquots and "SG" refers to D_e determination using single grains.

[2]"N accepted" refers to the number of multi-grain aliquots or single grains measured in the sample that pass rejection criteria. See Supplementary Material for details.

[3]"OD" refers to the overdispersion of the D_e distribution as calculated using the Central Age Model of Galbraith et al. (1999).

[4]Dose rates (Gy/ka) were calculated using the conversion factors of Liritzis et al. (2013) and are shown to 2 decimal places; ages were calculated prior to rounding. A maximum water content of 2 ± 1% (expressed as the percentage of the mass of dry sediment) was used in age calculations for all samples except for CL-16-10, which was estimated to be 20 ± 10% owing to the field-measured water content and lacustrine field context. See Supplementary Material for details.

[5]The D_e value of each sample was calculated using the Central Age Model of Galbraith et al. (1999).

[6]All ages are corrected for fading using the model of Huntley and Lamothe (2001) (see Supplementary Material for details). Ages are rounded to the nearest 10 years and are reported in thousands of years before 2018 and 2015, for the KTM and Sand Ramp samples, respectively.
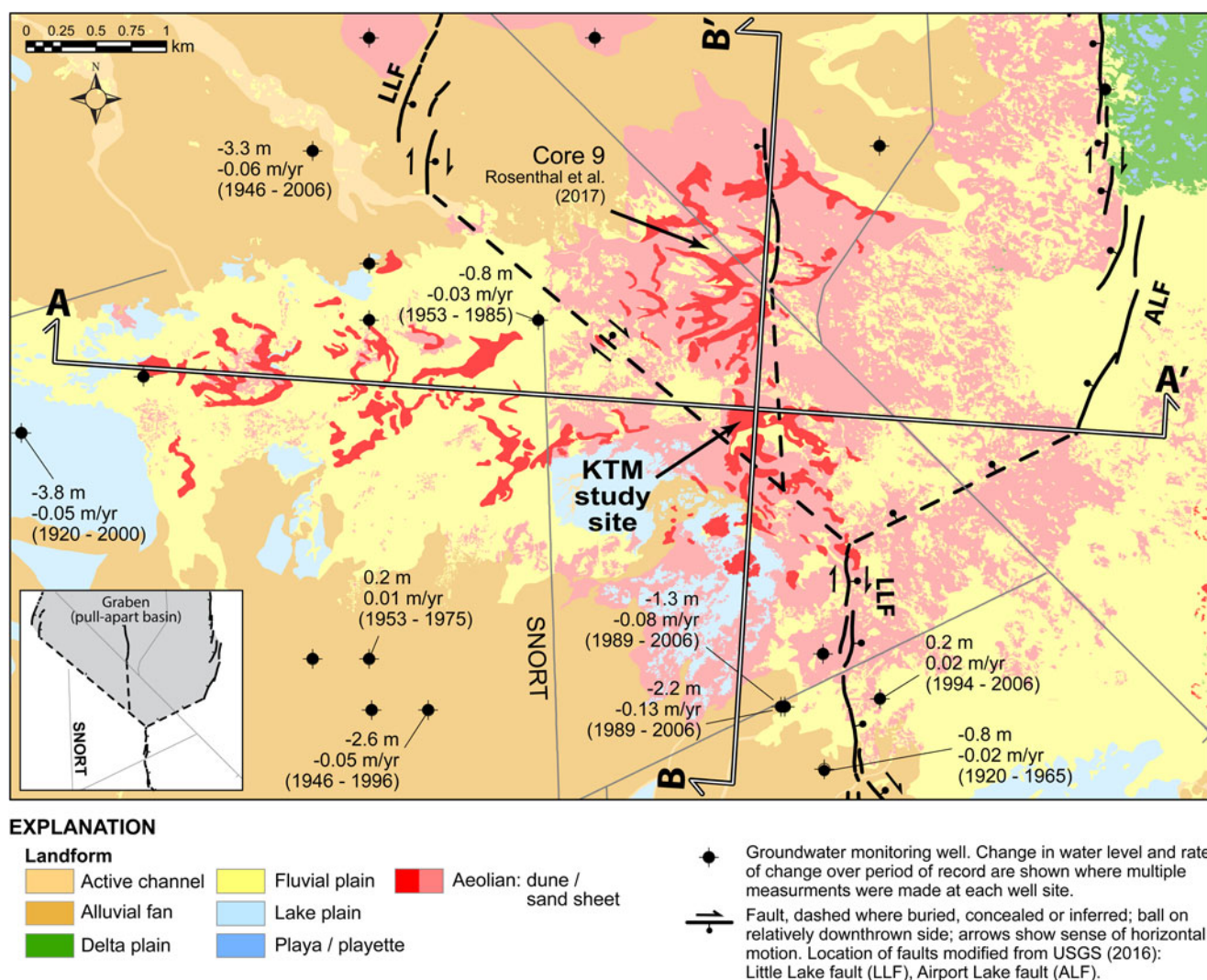
Figure 3. Landform and fault map of the western dune field showing the location of the KTM study site and graben of the Little Lake-Airport Lake fault zones (see inset) within the southern axial drainage system in China Lake basin (see Fig. 2). An array of groundwater monitoring wells bounding the LLF and change in water levels and rate of change over specific periods are shown. The rate of change in water levels from wells that are within 200 m of the LLF tend to have values that are nearly half of what is measured in wells that are located greater than 440 m west of the LLF, indicating the LLF-ALF zone acts as a barrier to horizonal groundwater flow. Transects A-A' and B-B' for geologic cross sections (see Fig. 4) across the western dune field are also shown.

Parabolic dunes in the area of the KTM study site are oriented with arms parallel to westerly winds and lie downwind (east) of areas of fluvial deposition and active channels that form the distal end of an extensive channel system sourced from the subbasin of El Paso Valley (Figs. 1, 2). These streams are the primary source of sediment that is readily available for aeolian transport. The dunes also act as barriers to fluvial activity. For example, active, slightly incised channels are diverted around the northern end of the study site dune-ridge complex where active channels within areas of thin sand sheets commonly terminate between the arms of parabolic dunes (Fig. 3).

The western dune field consists mostly of small (1–3 m high) parabolic dunes with arms as much as 100 m long. Two larger (3–8 m high) lobate parabolic dunes with arms up to 400 m long in the eastern margin of the dune field (Fig. 3) appear to have developed by coalescence of several smaller dunes. Approximately 400 m south of these dunes, a major N-S oriented dune ridge representing the "head" of a lobate parabolic dune

rises up to 6 m above the surrounding area. This dune ridge has been breached in the vicinity of the KTM study site, leading to the development of a series of nested elongated parabolic ridges that extend for up to 400 m to the east. A series of small (2–3 m high and 100–300 m long), NW-SE trending dune ridges spaced ~50 m apart are situated farther east of the KTM site (Fig. 3; Fig. 4, Transect A). Similar but shorter and discontinuous ridges (<100–200 m long) occur to the west and south of these dunes, also on a NW-SE trend. Dunes within the western margin of the dune field consist of irregular sinuous ridges and low parabolic dunes, with the "head" to the east and "arms" extending up to 300 m to the west (Fig. 3). The alignment of all dunes indicates that they were formed by winds from the west and southwest. In addition to the dunes, a broad expanse of an up to ~1-m-thick sand sheet accumulated adjacent to the LLF zone and the higher-relief vegetated dunes (Fig. 3).

All dune areas in the western dune field are partially to completely stabilized by vegetation and exhibit very low or
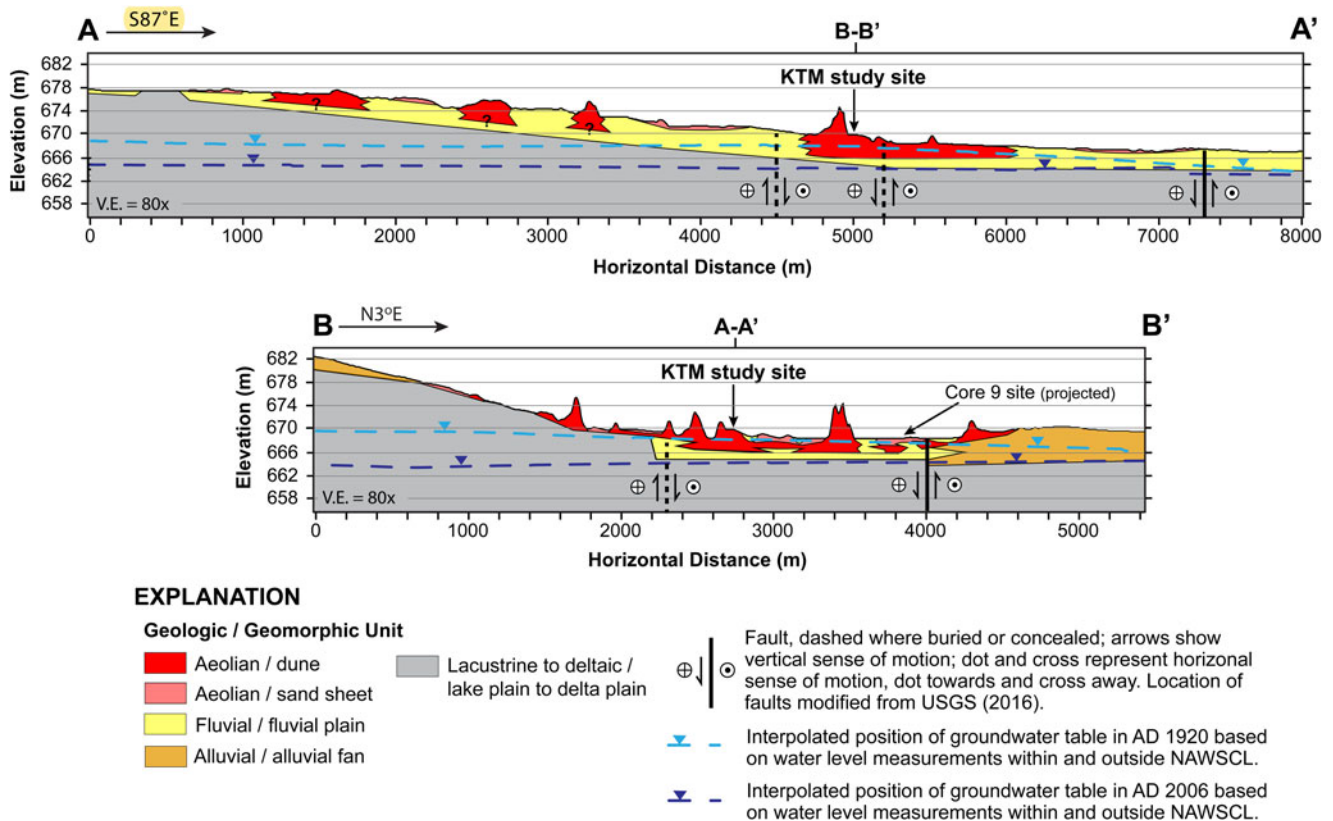
Figure 4. Geologic cross sections oriented on a west-east transect (A-A') and south-north transect (B-B') across the western dune field and KTM study site showing that the distribution of large, vegetated dunes is controlled primarily by high groundwater conditions within the southern axial drainage system and graben of the Little Lake and Airport Lake fault zones. The subsurface geology shown on the cross sections is based on observed stratigraphic exposures in a deep trench at the KTM study site, descriptions from a nearby ~10.7-m-deep sediment core (Core 9 of Rosenthal et al., 2017), inferences from mapped geomorphology, and location of faults. Changes in the shape of hydraulic head profiles based on interpolated groundwater levels in the area from nearby monitoring wells for the years AD 1920 and 2006 are shown.

negligible areas characterized by active sand transport. Aerial photographic evidence suggests that the western dune field system has not changed significantly since AD 1948, and, in general, is becoming more stable over time, although local anthropogenic disturbance (e.g., east of the KTM study site) has caused significant local change and active transport. The vegetated dunes within the LLF-ALF graben are the largest. These features have mostly parabolic forms with active slip faces and exhibit relief of up to ~8 m. Generally, the dunes have a lobate form (length/width ratio 1:3), indicating a relatively low rate of downwind migration (Pye and Tsoar, 1990). They are covered by a well-established, groundwater-dependent (phreatophytic) greasewood (*Sarcobatus vermiculatus*) and alkali sacaton (*Sporobolus airoides*) plant community—a vegetation community that is sensitive to relative changes in groundwater levels (e.g., Elmore et al., 2003). In contrast, the area of vegetated dunes along the axis of the fluvial plain west of the graben has less relief and is less vegetated. Active (bare, mobile) sand was observed in several localities, most prominently on the head of parabolic dunes adjacent to the KTM study site, and locally on the dune ridges to the south and east of this area (Fig. 3).

The eastern dune field, including the Sand Ramp site, is comprised of extensive sparsely vegetated sand sheets overlying colluvial and alluvial fan deposits on the southwestern piedmont of the Argus Range. Climbing dunes are formed adjacent to the mountain front. Adjacent to the China Lake playa, and along the PRF,

areas of localized groundwater discharge result in small areas of vegetation-anchored dunes (nebkhas).

Active ground deformation on the Little Lake fault

Understanding the extent and style of active ground deformation in Indian Wells Valley provides information to accurately interpret the landscape evolution of China Lake basin and the location of the western dune field. In some seismically active areas, ground deformation is commonly associated with discrete movements on faults during either coseismic slip or interseismic creep, or both. The area of Indian Wells Valley that the LLF and ALF cross is actively deforming. This is based on geodetic data from repeat, high-resolution leveling surveys of the north-south oriented, 6.55 km long Supersonic Naval Ordnance Research Track (SNORT) alignment within NAWSCL located immediately west of the western dune field (Zellmer and Roquemore, 1997) (Fig. 3). The style and magnitude of historical surface deformation of the SNORT alignment reflects complex fault geometry between the LLF and ALF, and possibly an underlying shallow (~3 km deep) magma body (Zellmer and Roquemore, 1997). The intersection of the LLF and ALF occurs ~2.1 km east of northern end of SNORT. Here, the two faults bifurcate to form a graben (Figs. 3, 4). The dominant style of coseismic deformation within the graben during surface-rupturing events is permanent surface subsidence, whereas interseismic deformation is reflected

by cyclic strain accumulation in the form of aseismic creep that produces periods of episodic uplift and subsidence (Zellmer and Roquemore, 1997; Fig. 3). Long-term and permanent surface subsidence from paleoseismic rupture events in this area has created accommodation space for fluvial and aeolian deposition.

Hydrogeomorphic profiles

All available data from groundwater-monitoring wells in western Indian Wells Valley for the years AD 1920 and 2006 were used to estimate groundwater conditions in the western dune field. Interpolated groundwater levels in areas of the western dune field were projected onto two geologic cross sections oriented longitudinal (A–A') and transverse (B–B') to the broad fluvial plain of the southern axial drainage system to aid in understanding the geomorphology in the area in relation to long-term changes in shallow groundwater conditions and active faulting (Figs. 3, 4). The subsurface geology shown on the cross sections is based on observed stratigraphic exposures at the KTM study site, descriptions from a nearby ~10.7-m-deep sediment core (Core 9; Rosenthal et al., 2017), inferences from mapped geomorphology, and location of faults modified after USGS (2016).

Before significant water development in the valley, the interpolated water table in the area of the western dune field in AD 1920 was close to or intersected the surface coinciding with the graben formed by the LLF and ALF. Phreatophyte vegetation communities dominated by greasewood, as in the western dune field, typically occur where depth to the water table is 3–4 m (Elmore et al., 2003). The interpolated groundwater table in AD 2006 shows that continued groundwater development by this time resulted in a lowering of the water table within the LLF-ALF graben of 4–6 m, likely affecting the vegetation community and thereby the potential stability of the vegetated dunes (Fig. 4).

Stratigraphic and chronologic investigations: KTM site

The KTM study site is located within the western dune field and consists of a wide, ~10-m-deep trench excavated through a ~6-m-high dune ridge and extended to a depth of ~4 m below local ground surface (Fig. 5). The morphology of the dunes in the immediate vicinity of the KTM study site was studied using a series of aerial photographs dating back to AD 1948. The AD 1948 images show the dunes prior to the breaching of the main dune ridge and excavation of the trench. The AD 1948 image shows that the main N-S oriented dune ridge is part of a large lunate, filled parabolic dune and appears to transgress two areas of low lobate parabolic dunes, interpreted to be an older generation of dunes to the east of the main dune ridge. The remnants of these older dunes are visible on contemporary images of the area, between the main dune ridge and a series of nested parabolic dunes that have formed since the AD 1970s, probably as a result of excavation of the trench and breaching of the western N-S oriented dunes (e.g., Fig. 5A).

The sedimentology, stratigraphy, and soil-geomorphology of deposits exposed in trench walls were studied and sampled for luminescence analysis at three locations (Figs. 5A, 6). The lower part of the aeolian deposits (Unit 1) was described at the KTM-east (north) locality at an elevation between 665 and 667 m (Fig. 5C). The sediment exposed here includes up to 2 m of massive fine- to medium-grained aeolian silty sand, with sub-planar stratification and weak cross bedding, as well as stage 1 to 1+ calcium carbonate accumulation in the soil profile.

Based on the topographic and stratigraphic position of the KTM east (north) exposure, these sandy sediments are likely the oldest aeolian deposits at the study site, and probably represent the lowermost sediments of the lobate parabolic dunes that were located east of the main N-S dune ridge (Fig. 5A). The aeolian sands of Unit 1 overlie a well-developed buried soil formed on ~1-m-thick sandy silt to silty clay, which is interpreted to be a flood plain (playa) deposit. The lower contact of the flood plain deposit represents an erosional boundary (e.g., ravinement surface) that formed on relatively older, massive to thinly interbedded, silty clay lacustrine to sandy silt fluvial-deltaic deposits associated with past water levels of China Lake (Fig. 6).

The upper part of the dune stratigraphy (Unit 2) at the trench site was described at the KTM west locality at elevations between 669 and 674 m, centered on the main N-S dune ridge (Fig. 5A). Sediments consists of 5 m of very pale brown fine- to medium-grained aeolian sand (Figs. 5B, 6). The sands are dominantly massive, with finely disseminated calcium carbonate (Stage 1) and weak sub-planar laminae and cross stratification at some levels. The lower part of these sediments appears to be slightly indurated.

An additional exposure of dune deposits was described at the KTM east (south) locality at an elevation near 668 m (Fig. 5A). About 1 m of massive, poorly sorted medium-grained aeolian sand with weak development of sub-planar stratification is exposed at this location (Fig. 5D). The upper 0.3 m of the exposure exhibits bioturbation, and prominent roots occur down to a depth of 0.55 m. Based on their composition, these sediments are assigned to Unit 2, but they are not part of the main dune ridge, and possibly represent the reworking of parts of Unit 1.

Stratigraphic and chronologic investigations: Sand ramp site

Sandy deposits associated with a relatively thin and expansive sand sheet over a hillslope of bedrock highlands at an elevation of ~670 m were described and sampled for luminescence dating (Figs. 2, 7). The study site includes a gully exposure of a ~3–4 m section of sandy sediment underlain by mostly sub-rounded to subangular fine to coarse gravel and boulders (Fig. 7). The sandy unit consists of a thin layer of loose sand associated with the active sand sheet at the site that is underlain by fine- to medium-grained silty sand with sub-planar stratification and cross bedding, and stage 1 to 1+ carbonate soil development. A few pebbly stringers and fluvial-type cross beds also were observed within the sandy unit. The gravel unit is moderately to well sorted and well cemented with depositional carbonate from past lake levels, and interpreted to be part colluvial and part lacustrine in origin (Fig. 7).

The geomorphic setting and sedimentology of the sandy unit indicate deposition within a sand ramp. Sand ramps are formed when aeolian sediment is trapped against a topographic barrier that, in turn, actively contributes to sediment accumulation, where the sand ramps commonly contain varying proportions of aeolian, hillslope, and fluvial sediments (Lancaster and Tchakerian, 1996; Rowell et al., 2018).

Aeolian sedimentology

At the KTM study site, dune sands range widely in mean grain size and sorting. Mean grain size of Unit 2 ranges between 1.90–2.79 phi (144–292 μm), with phi sorting coefficients of 0.61–0.92 (moderately to moderately well sorted). Unit 1 is similarly variable with a mean grain size of 1.84–2.90 phi, 129–280 μm; and
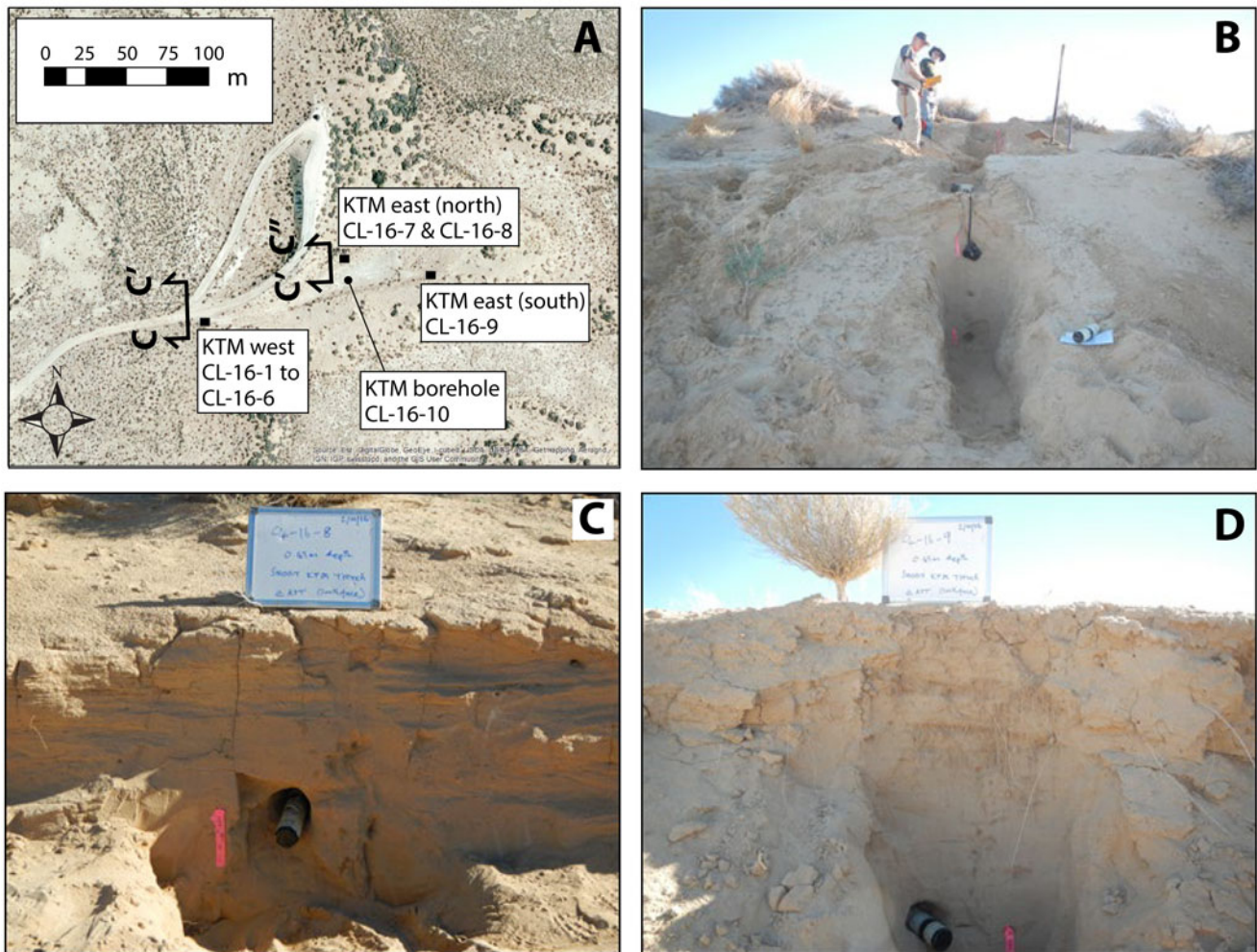
Figure 5. Photographs of the KTM study site: (A) aerial view of stratigraphic sections described within the KTM trench; (B) KTM west stratigraphic section locality showing benches excavated into the trench wall and post-infrared stimulated luminescence (post-IR-IRSL) sample (CL-16-1 to CL-16-6) locations; (C) KTM east (north) stratigraphic section locality showing aeolian deposits and post-IR-IRSL sample (CL-16-8) location; and (D) KTM east (south) stratigraphic section locality showing extensive bioturbation within the upper 0.55 m of the exposure and post-IR-IRSL sample (CL-16-9) location below 0.55 m within aeolian sandy sediments. Transect C-C'-C" for the geologic cross section (see Fig. 6) along the dune crest and across the KTM trench is also shown.

moderate to moderately well sorted. All the dune sediments contain silt and clay, with percentages ranging from 6–12%. The highest content of silt and clay is found in Unit 1 (7–12%). Carbonate content ranges from 5–8%. Generally, the particle size and sorting characteristics of sand at the KTM study site are similar to those of nearby dunes adjacent to Owens Lake (Lancaster et al., 2015; Fig. 1).

Bulk XRD analyses of grain mineralogy show that the dune and sand ramp sediments are composed of 28–42% quartz, 36–46% plagioclase, 10–13% K feldspar, and 6–15% calcite. The relative proportions of quartz, plagioclase, and K-feldspar in the sand indicate that they are derived from a local granodiorite source rock, which is the predominant igneous rock type in the nearby Sierra Nevada and El Paso mountains, and the core of the Coso Range (Hollett et al., 1991). The sand is similar in composition to that found in nearby dunes around Owens Lake (Fig. 1), and across much of the Mojave Desert (Lancaster et al., 2015). The high percentage of feldspar is also consistent with very short transport distances from source area to deposit site and a relatively short residence time in the fluvial and aeolian depositional environments (Muhs, 2017).

Luminescence dating

Luminescence ages (Table 1) from the KTM site dune sediments described above are in stratigraphic order, within 1-σ errors except for sample CL-16-9, which was collected ≥50 m east of all other samples (Figs. 5a, 6). The slight age and dose rate variations observed with depth at the KTM site can be attributed to heterogeneity in the dose rate of the sediments surrounding the sample tubes in the field; these would not have been taken into account in our dose rate estimates from sediments inside the tubes (see Supplementary Material for details on dose rate measurements). Ages of sands range from 2.12 ± 0.13 to 0.91 ± 0.06 ka and fall into two groups: (1) 2.12 ± 0.13 to 1.99 ± 0.14 ka and (2) 1.17 ± 0.07 to 0.91 ± 0.06 ka (Table 1). Each group is closely correlated with the two sedimentary units identified above. Thus, Unit 1 accumulated rapidly between ca. 2.1 and 2.0 ka and Unit 2 between ca. 1.2 and 0.91 ka.

In general, the post-IR-IRSL ages accord well with the described dune stratigraphy and soils. The stratigraphy and supporting ages indicate two distinct periods of sand accumulation at the site: an earlier period at 2.1 ± 0.1 to 2.0 ± 0.1 ka and a later period at 1.2 ± 0.1 to 0.91 ± 0.1 ka. The entire package of
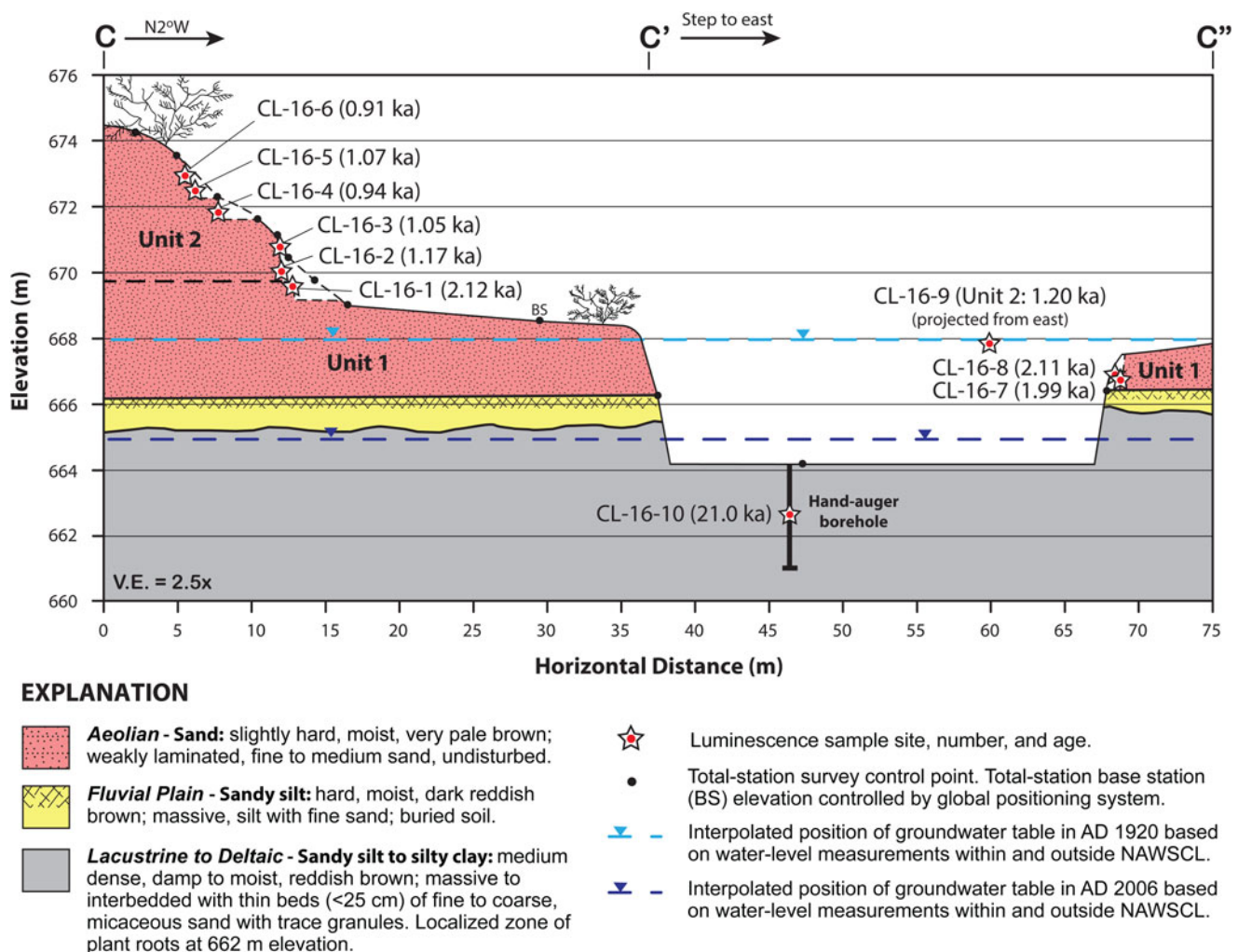
Figure 6. Composite geologic cross section of the KTM study site showing the vertical stratigraphic position of aeolian, flood plain (playa), and lacustrine to deltaic depositional units identified and described in trench walls. The location, sample numbers, and post-infrared stimulated luminescence (post-IR-IRSL) ages of samples are shown (see Table 1). The location of a hand-auger borehole placed at the bottom of the trench is also shown, as are the interpolated surfaces of the local groundwater table in AD 1920 and 2006 from nearby monitoring wells.

Late Holocene aeolian deposits is underlain by flood plain deposits capped by a buried soil. These flood plain deposits are, in turn, underlain by lacustrine to fluvio-deltaic deposits that yielded a post-IRIR$_{225}$ age of 21.0 ± 1.9 ka from the borehole at an elevation of 662.5 m (Table 1; Fig. 6).

At the Sand Ramp study site, duplicate samples separated horizontally by ∼0.4 m near the base of the sandy deposit yielded post-IRIR$_{225}$ ages of 1.76 ± 0.16 and 1.63 ± 0.15 ka (Fig. 7), and are statistically equivalent within 1 σ. The Sand Ramp ages are significantly older than all ages from Unit 2 of the KTM site (at 1 σ), and significantly younger than all ages but one (CL-16-7) from Unit 1 of the KTM site. The ages and sedimentology at the Sand Ramp site indicate aeolian sand transport and subsequent accumulation on denuded bedrock surfaces occurred at ca. 1.70 ka (Table 1).

DISCUSSION

Influence of active faulting and hydrogeology on aeolian geomorphology

The tectonic geomorphology of the oblique-normal LLF, ALF, and PRF is clearly expressed in the lake basin. Prominent left stepovers along these fault systems have resulted in complex surface deformation consisting of localized areas of small, uplifted blocks and adjacent tectonic depressions, which provide accommodation space for aeolian and fluvial deposits. The primary faults in the valley cut basin-fill material to varying degrees and may act as barriers or conduits to groundwater flow (e.g., Hadley et al., 2020). Deformation along faults introduces permeability heterogeneity and anisotropy, which have important effects on processes such as regional groundwater flow. Fault zones have the capacity to be hydraulic conduits connecting shallow and deep aquifers, but simultaneously the fault cores of many faults often form effective barriers to horizontal flow (e.g., Bense et al., 2013). Previous studies have described many of the faults in Indian Wells Valley as flow barriers because of observed water-level differentials across the broad LLF zone (Bloyd and Robson, 1971; Dutcher and Moyle, 1973; Mallory, 1978; St.-Amand, 1986), whereas others have suggested the fault zone does not affect groundwater flow (Berenbrock and Martin, 1991) or that observed water-level differences are reconciled by stratigraphy (Steinpress et al., 1994). Our analysis of groundwater levels across the active LLF-ALF system supports previous studies
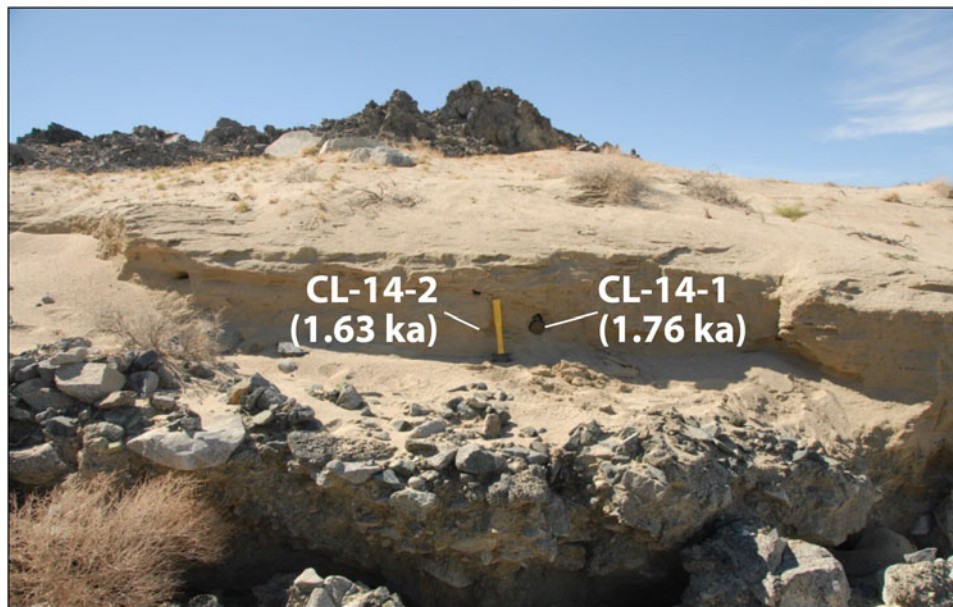
Figure 7. Photograph of the Sand Ramp study site showing a gully exposure at an elevation of ~669 m (see Fig. 2 for location). Samples for analysis by post-infrared stimulated luminescence (post-IR-IRSL) dating were collected at the base of sandy aeolian deposits adjacent to sledge hammer.

in the valley that suggest that the fault systems exert a major control on the hydrogeology of China Lake basin. We also show that the fault system has played an important role in controlling the aeolian geomorphology of the western dune field through its influence on supporting a well-established groundwater-dependent plant community, which is the primary vegetation type that stabilizes dunes in the basin (e.g., Fig. 4).

The interpolated groundwater tables from a closely spaced array of boreholes bounding the LLF-ALF graben in the western dune field provided a rare opportunity to identify changes between the shape of hydraulic head profiles in AD 1920 and 2006 across the fault zone (Fig. 4). The profile of the hydraulic gradient in AD 1920 (prior to groundwater resources development) is reflected by a subtle inflection (i.e., bulge) across the fault zone, whereas the profile in AD 2006 shows an overall change in gradient to the west. The long-term changes in groundwater level and rate of change are also relatively greater west of the LLF-ALF graben as a result of groundwater development in areas along the Sierra Nevada range front, whereas the rates are significantly lower within and east of the graben where ground water levels appear to have changed little over the 86 year period of record based on a network of wells with water-level measurements from specific years (Fig. 3). Furthermore, the presence of the large area of prominent vegetated dunes coincides with the subtle inflection in hydraulic gradient and the shallowest groundwater levels within the graben in AD 1920. The subtle inflection and shallow groundwater levels across the fault zone are likely influenced by a permeability structure that locally acts as a complex conduit-barrier system in which along-fault vertical and horizontal flow is allowed and across-fault flow is impeded (e.g., Bense et al., 2013; Hadley et al., 2020).

The lack of significant changes in groundwater levels within and east of the LLF-ALF graben, despite 86 years of groundwater development in Indian Wells Valley, indicates that the fault structure forms a groundwater barrier (e.g., St.-Amand, 1986). The hydrogeologic framework in areas of the LLF-ALF graben consists of facies changes between fluvial and lacustrine depositional environments along the margin of a fluctuating pluvial lake. Deep boreholes in the valley indicate that a thick section of mostly lacustrine fine-grained sediment is present within and east of the LLF, with its western margin interbedded with relatively thinner and coarse-grained alluvial and fan-delta layers (e.g., Kunkel and Chase, 1969; Dutcher and Moyle, 1973). The products of deformation processes accommodating strain in a fault zone can either reduce the permeability in the fault core or enhance permeability in the surrounding damaged zone. Permeability reduction across an entire shear zone, however, can occur from particulate flow, sediment mixing, and clay smear in unlithified rocks (e.g., Caine et al., 1996; Bense et al., 2013). Creep from interseismic strain accumulation and coseismic slip during surface rupture earthquakes on the LLF-ALF system or triggered slip on the LLF from earthquakes generated on the nearby PRF (e.g., DuRoss et al., 2020) likely promotes permeability reduction of aquifer materials within the shear zone. The juxtaposition of aquifer materials with different sediment textures also produces a lateral permeability contrast that can impede horizontal groundwater flow (e.g., Bense et al., 2013). Observations and modeling of the groundwater system in Owens Valley within the Owens River watershed, north of Indian Wells Valley (Fig. 1), has also shown that the active oblique-normal Owens Valley fault system can reduce transmissivity of fine-grained aquifer materials in the fault zone by a factor of 20—from ~1000–50 $(m^3/d)/m$ (Danskin, 1998). The net result of reducing the relative permeability of aquifer materials within the LLF shear zone from progressive deformation has preferentially influenced vertical groundwater flow, thereby producing localized elevated groundwater conditions, that in turn provide a steady source of moisture for a robust phreatophyte vegetation community in an otherwise arid environment.

Development of aeolian features

Stratigraphy, sedimentology, and luminescence dating of dune sands at the KTM and Sand Ramp study sites provide convincing

evidence for at least three centennial-scale episodes of aeolian sand accumulation in the China Lake basin during the Late Holocene (Fig. 8A). An early episode occurred from 2.1 ± 0.1 to 2.0 ± 0.1 ka (Unit 1) at the KTM site and is interpreted to represent a period of parabolic dune formation that initially developed over a fluvial plain and deltaic depositional environments. The fluvial sediments at the site have a moderately developed soil and are inferred to have been deposited soon after desiccation of pluvial China Lake by 11.1 ka (e.g., Rosenthal et al., 2017), which is supported by the age of deeper stratigraphy at the site, which is composed of deltaic deposits with an age of 21.0 ± 1.9 ka. A later period of sand accumulation at the KTM site from 1.2 ± 0.1 to 0.91 ± 0.1 ka (Unit 2) is associated with formation of the main N-S oriented dune ridge and reworking of older dune sand deposited during the earlier period. There is no evidence at the KTM site for any more recent aeolian sand accumulation, until the last 50 years from anthropogenic disturbance in the area.

The stratigraphy and luminescence dating of sandy sediments at the Sand Ramp site provide evidence for sand accumulation during an intervening period of sand transport from 1.8 ± 0.2 to 1.6 ± 0.2 ka in areas downwind of the western dune field and across the playa. At this site, the bedrock highlands form an obstacle that has influenced aeolian sand deposition and alluvial reworking, which has preserved a Late Holocene record of sand transport in the area. The youngest luminescence date from Unit 1 at the KTM site of 1.99 ± 0.14 ka and the oldest date from the Sand Ramp site of 1.76 ± 0.16 ka overlap within their uncertainties, thereby precluding separation of the deposits into two distinct episodes of sand accumulation based on the kernel probability density function (Fig. 8A). In light of the aeolian and lake-level records from nearby Owens Lake basin, as well as the other dates at both sites that do not overlap, we argue that there is good evidence to support the separation of an intermediate episode of sand accumulation centered at ca. 1.7 ka in response to high-frequency changes in hydroclimate, which are explained later (e.g., Fig. 8C). Nonetheless, the new IRSL ages of the sand dune and sand ramp deposits provide limiting ages for the vegetated sand dunes and inactive sand sheets to less than ca. 2 ka in the western dune field and downwind areas. It is possible, however, that aeolian features in the eastern dune field and farther to the east on the piedmont slopes of the Argus Range may be older (Figs. 1, 2).

The boundary conditions leading to the formation of dunes in China Lake basin can be evaluated in terms of the sediment state model (Kocurek and Lancaster, 1999). In this conceptual model, a source of sand-sized sediment that is available for transport by the wind (i.e., not stabilized by vegetation or high groundwater levels) is needed. Wind energy must be sufficient to transport the sand to the deposition area, where some combination of a decrease in wind energy, increased vegetation cover, or topographic obstacle results in decreased sediment transport rates, and deposition of sand. The potential for dune formation may be enhanced in periods when sand supplied during periods of wetter climates is reworked into dunes during subsequent drier periods.

The mineral composition of the dune sand at the KTM and Sand Ramp study sites indicates a primary sediment source in the granitic rocks of the Sierra Nevada, ~15 and ~25 km west of the dunes. Fluvial transport of sand to the distal parts of the primary axial drainages in Indian Wells Valley likely was associated with extreme flood events due to enhanced winter subtropical moisture in the region (e.g., Enzel et al., 1989; Enzel and Wells, 1997; Miller et al., 2010). Sand deposited by fluvial

processes was then reworked by wind and transported eastwards towards areas of greater subsurface moisture and vegetation growth in a similar way to parabolic dune formation at White Sands National Monument (Langford et al., 2009; Reitz et al., 2010). The occurrence of parabolic dunes in the KTM study area indicates that vegetation was present when they formed. In China Lake basin, the greater vegetation cover was likely promoted by the occurrence of relatively fresh to brackish groundwater at shallow depth, related to areas of faulting. As the dunes interact with vegetation, the rate of sand movement decreases, allowing vegetation to colonize the dune, which tends to evolve towards a parabolic form. Spatial correspondence between vegetated dunes and faulting in the western dune field is reflected in areas with the best-developed, high-relief parabolic dunes that have formed along a linear trend coinciding with the northerly strike of a short fault splay within the LLF-ALF graben in the area between the KTM study site and the sediment Core 9 site (Figs. 3, 4).

Comparison of spatiotemporal patterns of aeolian sand accumulation in China Lake basin with regional records

Comparison of the ages of periods of dune formation in China Lake basin with the luminescence-dated record of dune accumulation in the adjacent areas of the Mojave and Great Basin deserts reveals overlap with these records across a range of latitude (Fig. 8B). The period ca. 1–2 ka apparently was one of widespread aeolian accumulation throughout the Great Basin and Mojave deserts. In many cases, dunes and sand ramps were fed by sand from adjacent playa and/or alluvial sources. In the Great Basin, cross-bedded dune sands were deposited adjacent to Owens Lake at 1.71 ka (Lancaster and Bacon, 2012) and at Ash Meadows in southwestern Nevada at 1.58 ka (Lancaster and Mahan, 2012), which both overlap with the age of sand accumulation at the Sand Ramp site from 1.8 ± 0.2 to 1.6 ± 0.2 ka (Fig. 8). In the Mojave Desert, sand ramps accumulated against the west side of the Cronese Mountains at ca. 1.7–1.5 ka and ca. 2.0–2.2 ka (Lancaster and Tchakerian, 2003), fed by sand from the west Cronese playa and overlap with the episode of sand accumulation at the Sand Ramp site and the age of Unit 1 at the KTM site, respectively. Unit XIV of the Kelso Dunes formed ca. 1.54–1.60 ka and at ca. 2.06 ka (Lancaster and Tchakerian, 2003), likely fed by sand from the Granite Mountains alluvial fans (Muhs et al., 2017), which also overlaps with the age of sand accumulation at the KTM and Sand Ramp sites. River-source bordering dunes in the Gila River Valley of Arizona formed between ca. 1.36 and 1.95 ka (Wright et al., 2011), having temporal correspondence with the age of sand accumulation in China Lake basin. The age of later aeolian sand accumulation (Unit 2) at the KTM site at 1.2 ± 0.1 to 0.9 ± 0.1 ka, however, is not represented at any other location in the region, except locally in the Owens River watershed (Fig. 1), where sand accumulated at the margin of Owens Lake at 1.13 ± 0.9 ka (Lancaster and Bacon, 2012) (Fig. 8B).

The episodes of aeolian sand accumulation in China Lake basin also can be compared to the detailed Late Holocene lake-level record of nearby Owens Lake to aid in linking aeolian accumulation to hydroclimate variability in the southern Sierra Nevada (Bacon et al., 2018; Figs. 1, 8C). The early episode of sand accumulation at 2.1 ± 0.1 to 2.0 ± 0.1 ka in China Lake basin coincides with the transition between low lake levels at 2.10 ± 0.03 cal ka BP and relatively high lake levels at 2.01 ± 0.06 cal ka BP of Owens Lake. The age of sand accumulation at
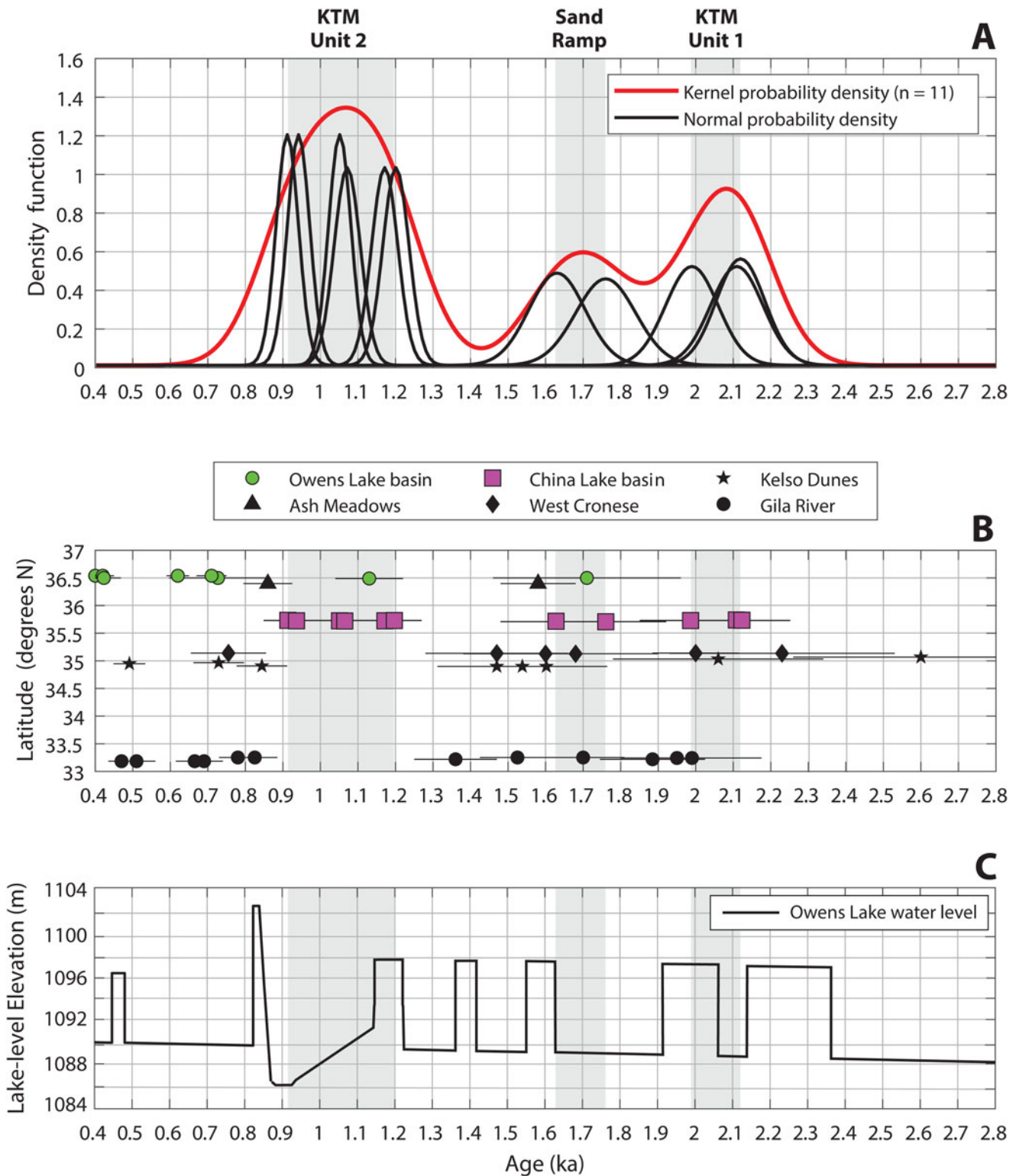
Figure 8. Plots showing: (A) kernel and normal probability density functions of luminescence ages of aeolian deposits from sites of this study that display clustering of ages and define three periods of aeolian accumulation in China Lake basin (gray shaded bars); (B) comparison of the spatiotemporal correspondence of aeolian accumulation in China Lake basin with other well-dated sites in the Intermountain West for the period 2.8–0.4 ka; luminescence ages for other sites from INQUA Dunes Atlas Chronologic Database and contributing publications (see text for references); and (C) Late Holocene water-level record of Owens Lake based on the integration of sediment lake core data and shoreline chronology with wind-wave and sediment entrainment modeling of lake-core sedimentology (Bacon et al., 2018) that shows temporal correspondence between the transition of high to low lake levels and mean ages of sand accumulation in China Lake basin.

the Sand Ramp site from 1.8 ± 0.2 to 1.6 ± 0.2 ka also coincides with another period of oscillating water levels corresponding to the end of an extended period of low lake levels at 1.79 ± 0.17 cal ka BP and transition to high lake levels at 1.59 ± 0.30 cal ka BP (Fig. 8). The good temporal correspondence between the age of sand accumulation at the Sand Ramp site and low water levels of Owens Lake, along with the ca. 1.71 ka age of sand dunes in Owens Lake basin, collectively supports the separation of an intermediate episode of sand accumulation in China Lake basin. Furthermore, the early and intermediate episodes of sand accumulation in China Lake basin coincide with the end of persistent drought across the central Great Basin from 2.8–1.85 ka inferred primarily from pollen records and referred to as the Late Holocene Dry Period (Mensing et al., 2013).

The latest episode of sand accumulation identified in China Lake basin at ca. 1.2 ± 0.1 to 0.9 ± 0.1 ka follows a similar trend of corresponding to periods of low lake levels where sand accumulation occurred at the transition between high lake levels at 1.18 ± 0.04 cal ka BP and the severe drying and contraction of Owens Lake at 0.97 ± 0.17 cal ka BP (Bacon et al., 2018; Fig. 8). The sand accumulation from ca. 1.2–0.9 ka in China Lake basin and contraction of Owens Lake at this time occurred during the first period of extreme and persistent drought during the Medieval Climatic Anomaly (MCA-1 or Stine #1) identified in the south-central Sierra Nevada and western U.S. (e.g., Stine, 1994; Cook et al., 2010). The coincidence of geomorphic change in China Lake and Owens Lake basins is consistent with a hydrologic link between sand accumulation and enhanced runoff, where sand likely began to accumulate from deflation of less-active fluvial plains and exposed lake beds at the transitions to more arid hydroclimate conditions in the southern Sierra Nevada that influenced low (or near desiccation) lake levels.

The importance of sediment supply as a control on periods of aeolian accumulation in the southwestern U.S. has been highlighted by Halfen et al. (2015). It appears that the Late Holocene China Lake aeolian record further supports this model. In this case, sand transported to distal alluvial fan or playa margin locations during periods of enhanced runoff from Sierra Nevada watersheds was reworked by the wind either contemporaneously or as lagged input (e.g., Kocurek, 1998) to form parabolic dunes and sand ramps. Later periods of aeolian activity likely were associated with reworking of the primary deposits at the transitions between wetter and drier periods, but also with some additional input from enhanced runoff and transport due to continued Late Holocene hydroclimate variability.

CONCLUSIONS

Late Holocene aeolian deposits and landforms in the China Lake basin developed in the context of active tectonism and hydroclimate variability. Active tectonics in China Lake basin produced a unique, yet geomorphically sensitive, setting conducive to the accumulation of aeolian deposits and stabilization of dune fields through their influence on local groundwater levels. In particular, groundwater barriers resulting from the complex fault geometries associated with the LLF-ALF graben and PRF shear zones resulted in localized areas of preferential vertical flow that influences higher groundwater levels and spring discharge capable of supporting dune-stabilizing vegetation in the western and eastern dune fields. Hydroclimatic variability has influenced the supply of sand-sized sediment derived from granitic terrains to the basin floor during periods of enhanced rainfall and runoff. This sediment was subsequently reworked by winds to form dunes and sand sheets at 2.1 ± 0.1 to 2.0 ± 0.1 ka, 1.8 ± 0.2 to 1.6 ± 0.2 ka, and 1.2 ± 0.1 to 0.9 ± 0.1 ka. Although climatic conditions in the basin are conducive to aeolian activity, recent sand movement is mostly confined to areas of anthropogenic disturbance, suggesting the importance of sediment supply to dune formation in this area.

REFERENCES

Amos, C.B., Brownlee, S.J., Rood, D.H., Burch Fisher, G., Bürgmann, R., Renne, P.R., Jayko, A.S., 2013. Chronology of tectonic, geomorphic, and volcanic interactions and the tempo of fault slip near Little Lake, California. *Geological Society of America Bulletin* **125**, 1187–1202.

Arnold, L.J., Roberts, R.G., 2009. Stochastic modelling of multi-grain equivalent dose (*De*) distributions: implications for OSL dating of sediment mixtures. *Quaternary Geochronology* **4**, 204–230.

Bacon, S.N., Bullard, T.F., Adams, K.D., Decker, D.L., 2019. *Geomorphic Map of China Lake Basin Below 700 m Elevation, Inyo, Kern, and San Bernardino Counties, California*. Prepared by Naval Earth Sciences and Engineering Program, Desert Research Institute for Naval Air Warfare Center, Weapons Division, China Lake. NAWCWD TP 8839, 1:50,000-scale.

Bacon, S.N., Jayko, A.S., Owen, L.A., Lindvall, S.C., Rhodes, E.J., Schumer, R.A., Decker, D.L., 2020. A 50,000-year record of lake-level variations and overflow from Owens Lake, eastern California, USA. *Quaternary Science Reviews* **238**, 106312. https://doi.org/10.1016/j.quascirev.2020.106312.

Bacon, S.N., Lancaster, N., Stine, S., Rhodes, E.J., McCarley Holder, G.A., 2018. A continuous 4000-year lake-level record of Owens Lake, south-central Sierra Nevada, California, USA. *Quaternary Research* **90**, 276–302.

Bense, V.F., Gleeson, B.,T., Loveless, S.E., Bour, O., Scibek, J., 2013. Fault zone hydrogeology. *Earth-Science Reviews* **127**, 171–192.

Berenbrock, C., Martin, P., 1991. The ground-water flow system in the Indian Wells Valley, Kern, Inyo, and San Bernardino counties, California. *U.S. Geological Survey Water Resources Investigations Report* 89-4191, 81 pp.

Blott, S.J., Pye, K., 2001. GRADISTAT: a grain size distribution and statistics package for the analysis of unconsolidated sediments. *Earth Surface Processes and Landforms* **26**, 1237–1248.

Bloyd, R.M., Robson, S.G., 1971. Mathematical groundwater model of Indian Wells Valley, California. *U.S. Geological Survey Open-File Report* 72-41, 36 pp.

Bryant, W.A., Hart, E.W., 2007. Fault-rupture hazard zones in California. *California Geological Survey Special Publication* 42, 46 pp.

Bullard, T.F., Bacon, S.N., Adams, K.D., Decker, D.L., 2019. *Geomorphic Map of the China Lake Basin Below 700 m in Support of Cultural Resource Management at Naval Air Weapons Station China Lake*. Prepared by Naval Earth Sciences and Engineering Program, Desert Research Institute for Naval Air Warfare Center, Weapons Division, China Lake, NAWCWD TP 8839, 79 pp.

Caine, J.S., Evans, J.P., Forster, C.B., 1996. Fault zone architecture and permeability structure. *Geology* **24**, 1025–1028.

Cook, E.R., Seager, R., Heim, Jr. R.R., Vose, R.S., Herweijer, C., Woodhouse, C., 2010. Megadrought in North America: placing the IPCC projections of hydroclimate change in a long-term paleoclimate context. *Journal of Quaternary Science* **25**, 48–61.

Danskin, W.R., 1998. Evaluation of the hydrologic system and selected water-management alternatives in the Owens Valley, California. *U.S. Geological Survey Water-Supply Paper* 2370, 175 pp.

Dokka, R.K., Travis, C.J., 1990. The role of the Eastern California shear zone in accommodating Pacific-North American plate motion. *Geophysical Research Letters* **17**, 1323–1326.

Dunne, G.C., Walker, J.D., 2004. Structure and evolution of the East Sierran thrust system, east central California. *Tectonics* **23**, TC4012. https://doi.org/10.1029/2002TC001478.

DuRoss, C.B., Gold, R.D., Dawson, T.E., Scharer, K. M., Kendrick, K.J., Akciz, S.O., Angster, S.J., et al., 2020. Surface displacement distributions for the July 2019 Ridgecrest, California, earthquake ruptures. *Bulletin of the Seismological Society of America* **110**, 1400–1418.

Dutcher, L.C., Moyle, W.R. 1973. Geologic and hydrologic features of Indian Wells Valley, CA. *U.S. Geological Survey Water Supply Paper* 2007, 30 pp.

Elmore, A.J., Mustard, J.F., Manning, S.J., 2003. Regional patterns of plant community response to changes in water: Owens Valley, California. *Ecological Applications* **13**, 443–640.

Enzel, Y., Cayan, D.R., Anderson, R.Y., Wells, S.G., 1989. Atmospheric circulation during Holocene lake stands in the Mojave Desert: evidence of regional climate change. *Nature* **341**, 44–48.

Enzel, Y., Wells, S.G., 1997. Extracting Holocene paleohydrology and paleoclimatology information from modern extreme flood events: an example from southern California. *Geomorphology* **19**, 203–226.

Epps, T.M., Britten, H.B., Rust, R.W., 1998. Historical biogeography of *Eusattis muricatus* (Coleoptera: Tenebrionidea) within the Great Basin, western North America. *Journal of Biogeography* **25**, 947–968.

Fryberger, S.G., Dean, G., 1979. Dune forms and wind regimes. In: McKee, E.D. (Ed.), A Study of Global Sand Seas. *U.S. Geological Survey Professional Paper* 1052, pp. 137–140.

Galbraith, R.F., Roberts, R.G., Laslett, G.M., Yoshida, H., Olley, J.M., 1999. Optical dating of single and multiple grains of quartz from Jinmium rock shelter, northern Australia: part I, experimental design and statistical models. *Archaeometry* **41**, 339–364.

Hadley, D.R., Abrams, D.B., Roadcap, G.S., 2020. Modeling a large scale historic aquifer test: insight into the hydrogeology of a regional fault zone. *Groundwater* **58**, 453–463.

Halfen, A.F., Lancaster, N., Wolfe, S.A., 2015. Interpretations and common challenges of aeolian records from North American dune fields. *Quaternary International* **410**, 75–95.

Hauksson, E., Hutton, K., Kanamori, H., Jones, L., Mori, J., Hough, S., Roquemore, G., 1995. Preliminary report on the 1995 Ridgecrest earthquake sequence in eastern California. *Seismological Research Letters* **66**, 54–60.

Hollett, K.J., Danskin, W.R., McCaffrey, W.F., Walti, C.L., 1991. Geology and water resources of Owens Valley, California. *U.S. Geological Survey Water-Supply Paper* 2370-B, B1–B77.

Huntley, D.J., Lamothe, M., 2001. Ubiquity of anomalous fading in K-feldspars and the measurement and correction for it in optical dating. *Canadian Journal of Earth Sciences* **38**, 1093–1106.

IWVGA [Indian Wells Valley Groundwater Authority], 2020. *Groundwater Sustainability Plan for the Indian Wells Valley Groundwater Basin*. Bulletin 118 Basin No. 6-054, 366 pp.

Jewell, P.W., Nicoll, K., 2011. Wind regimes and aeolian transport in the Great Basin, U.S.A. *Geomorphology* **129**, 1–13.

Kocurek, G., 1998. Aeolian system response to external forcing factors—a sequence stratigraphic view of the Saharan region. In: Alsharan, A.S., Glennie, K.W., Whittle, G.L., Kendall, C.G.S.C. (Eds.), *Quaternary Deserts and Climatic Change*. Balkema, Rotterdam/Brookfield, pp. 327–338.

Kocurek, G., Lancaster, N., 1999. Aeolian system sediment state: theory and Mojave Desert Kelso dune field example. *Sedimentology* **46**, 505–515.

Kunkel, F., Chase, G.F., 1969. Geology and ground water in Indian Wells Valley, California. *U.S. Geological Survey Open-File Report* 69-329, 84 pp.

Lancaster, N., 2020. Dunefields of the Southwest Deserts. In: Lancaster, N., Hesp, P. (Eds.), *Inland Dunes of North America*. Springer International Publishing, Cham, Switzerland, pp. 311–337.

Lancaster, N., Bacon, S.N., 2012. *Late Holocene stratigraphy and chronology of the Keeler Dunes area*. Report prepared by Desert Research Institute for Great Basin Unified Air Pollution Control District, 24 pp. https://gbuapcd.org/Docs/OwensLake/KeelerDunes/OriginAndDevelopment/Lancaster%20and%20Bacon%202012a_Late%20Holocene%20stratigraphy%20and%20chronology_Final20121116.pdf

Lancaster, N., Baker, S., Bacon, S., McCarley-Holder, G., 2015. Owens Lake dune fields: composition, sources of sand, and transport pathways. *CATENA* **134**, 41–49.

Lancaster, N., Mahan, S.A., 2012. Holocene dune formation at Ash Meadows National Wildlife Area, Nevada. *Quaternary Research* **78**, 266–274.

Lancaster, N., Tchakerian, V.P., 1996. Geomorphology and sediments of sand ramps in the Mojave Desert. *Geomorphology* **17**, 151–166.

Lancaster, N., Tchakerian, V.P., 2003. Late Quaternary eolian dynamics, Mojave Desert, California, in: Enzel, Y., Wells, S.G., Lancaster, N. (Eds.), *Paleoenvironments and Paleohydrology of the Mojave and Southern Great Basin Deserts*. Geological Society of America, Boulder, CO, pp. 231–249.

Langford, R.P., Rose, J.M., White, D.E., 2009. Groundwater salinity as a control on development of eolian landscape: an example from the White Sands of New Mexico. *Geomorphology* **105**, 39–49.

Liritzis, I., Singhvi, A. K., Feathers, J. K., Wagner, G. A., Kadereit, A., Zacharias, N., Li, S.-H., 2013. *Luminescence Dating in Archaeology, Anthropology, and Geoarchaeology – An Overview*. Springer Briefs in Earth System Sciences. Springer, Heidelberg. 70 pp.

Mallory, J.M., 1978. Water-level predictions for Indian Wells Valley groundwater basin. *U.S. Geological Survey Open-File Report* 79-254.

Mensing, S.A., Sharpe, S.E., Tunno, I., Sada, D.W., Thomas, J.M., Starratt, S., Smith, J., 2013. The Late Holocene Dry Period: multiproxy evidence for an extended drought between 2800 and 1850 cal yr BP across the central Great Basin, USA. *Quaternary Science Reviews* **78**, 266–282.

Miller, D.M., Schmidt, K.M., Mahan, S.A., McGeehin, J.P., Owen, L.A., Barron, J.A., Lehmkuhl, F., Lehrer, R., 2010. Holocene landscape response to seasonality of storms in the Mojave Desert. *Quaternary International* **215**, 45–61.

Monastero, F.C., Walker, J.D., Katzenstein, A.M., Sabin, A.E., 2002. Neogene evolution of the Indian Wells Valley, east-central California. In: Glazner, A.F., Walker, J.D., Bartley, J.M. (Eds.), Geologic Evolution of the Mojave Desert and Southwestern Basin and Range: *Geological Society of America Memoir* 195, 199–228.

Moore, J.G., Moring, B.C., 2013. Range wide glaciation in the Sierra Nevada, California. *Geosphere* **9**, 1804–1818.

Muhs, D.R., 2017. Evaluation of simple geochemical indicators of aeolian sand provenance: Late Quaternary dune fields of North America revisited. *Quaternary Science Reviews* **171**, 260–296.

Muhs, D.R., Lancaster, N., Skipp, G.L., 2017. A complex origin for the Kelso Dunes, Mojave National Preserve, California, USA: a case study using a simple geochemical method with global applications. *Geomorphology* **276**, 222–243.

Munroe, J.S., Gorin, A.L., Stone, N.N., Amidon, W.H., 2017. Properties, age, and significance of dunes near Snow Water Lake, Elko County, Nevada. *Quaternary Research* **87**, 24–36.

Murray, A.S., Wintle, A.G., 2000. Luminescence dating of quartz using an improved single-aliquot regenerative-dose protocol. *Radiation Measurements* **32**, 57–73.

Murray, A.S., Wintle, A.G., 2003. The single-aliquot regenerative dose protocol: potential for improvements in reliability. *Radiation Measurements* **37**, 377–381.

Pavlik, B.M., 1989. Phytogeography of sand dunes in the Great Basin and Mojave deserts. *Journal of Biogeography* **16**, 227–238.

Ponti, D.J., Blair, J.L., Rosa, C.M., Thomas, K., Pickering, A.J., Akciz, S., Angster, S., et. al., 2020. Documentation of surface fault rupture and ground deformation features produced by the Ridgecrest M6.4 and M7.1 earthquake sequence of July 4 and 5, 2019. *Seismological Research Letters* **91**. https://doi.org/10.1785/0220190322.

Pye, K., Tsoar, H., 1990. *Aeolian Sand and Sand Dunes*. Unwin Hyman, London.

Quade, J., 1986. Late Quaternary environmental changes in the upper Las Vegas Valley, Nevada. *Quaternary Research* **26**, 340–357.

Reitz, M.D., Jerolmack, D.J., Ewing, R.C., Martin, R.L., 2010. Barchan-parabolic dune pattern transition from vegetation stability threshold. *Geophysical Research Letters* **37**, L19402. https://doi.org/10.1029/2010GL044957.

Rhodes, E.J., 2015. Dating sediments using potassium feldspar single-grain IRSL: initial methodological considerations. *Quaternary International* **362**, 14–22.

Roquemore, G.R., Zellmer, J.T., 1987. *Naval Weapons Center Active Fault Map Series, NWC TP-6828*. Naval Weapons Center, China Lake, CA, 18 p., 14 maps, scale 1:24,000.

Rosenthal, J.S., Meyer, J., Palacios-Fest, M.R., Young, D.C., Ugan, A., Byrd, B.F., Gobalet, K., Giacomo, J., 2017. Paleohydrology of China Lake basin and the context of early human occupation in the northwestern Mojave Desert, USA. *Quaternary Science Reviews* **167**, 112–139.

Rowell, A.L.K., Thomas, D.S.G., Bailey, R.M., Holmes, P.J., 2018. Sand ramps as palaeoenvironmental archives: integrating general principles and regional contexts through reanalysis of the Klipkraal Sands, South Africa. *Geomorphology* **311**, 103–113.

Sherrod, L.A., Dunn, G., Peterson, G.A., Kolberg, R.L., 2002. Inorganic carbon analysis by modified pressure-calcimeter method. *Soil Science Society of America Journal* **66**, 299–305.

Shiyuan, Z., Ju, L., Whiteman, C.D., Xindi, B., Wenqing, Y., 2008. Climatology of high wind events in the Owens Valley, California. *Monthly Weather Review* **136**, 3536–3552.

St.-Amand, P., 1986. *Water Supply of Indian Wells Valley, California*. Naval Weapons Center Technical Publication 6404, 71 p.

Steinpress, M.G., Couch, R.F., McDonald, J., 1994. The China Lake barrier: a structural or stratigraphic hydrologic feature? *Geological Society of America Abstracts with Programs* **26**, 95.

Stine, S., 1994. Extreme and persistent drought in the Sierra Nevada/Western Great Basin during Medieval time. *Nature* **369**, 546–549.

Thompson Jobe, J., Philibosian, B., Chupik, C., Dawson, T., Bennett, S.E.K., Gold, R., DuRoss, C., et al., 2020. Evidence of previous faulting along the 2019 Ridgecrest earthquake ruptures. *Bulletin of the Seismological Society of America* **110**. https://doi.org/10.1785/0120200041.

Thomsen, K. J., Murray, A. S., Jain, M., Bøtter-Jensen, L., 2008. Laboratory fading rates of various luminescence signals from feldspar-rich sediment extracts. *Radiation Measurements* **43**, 1474–1486.

U.S. Geological Survey (USGS), 2016. *Quaternary Fault and Fold Database for the United States*. https://www.usgs.gov/natural-hazards/earthquake-hazards/faults. [accessed May, 2016]

Wesnousky, S.G., 2005. Active faulting in the Walker Lane. *Tectonics* **24**, TC3009. https://doi.org/10.1029/2004TC001645.

Wright, D.K., Forman, S.L., Waters, M.R., Ravesloot, J.C., 2011. Holocene eolian activation as a proxy for broad-scale landscape change on the Gila River Indian Community, Arizona. *Quaternary Research* **76**, 10–21.

Zellmer, J.T., Roquemore, G.R., 1997. Tectonic deformation of a supersonic naval ordnance research track, Indian Wells Valley, California. *Environmental and Engineering Geoscience* **3**, 205–215.